Supporting information

Synchro-Excited Free-Running Single Photon Counting:

A Novel Method for Measuring Short-Wave Infrared Emission Kinetics

Ching-Wei Lin,[†,§] Sergei M. Bachilo,[†] and R. Bruce Weisman[†,‡,*]

[†] Department of Chemistry and the Smalley-Curl institute, Rice University, Houston, TX 77005, United States

[‡] Department of Materials Science and NanoEngineering, Rice University, Houston, TX 77005, United States

[§] Present address: The David H. Koch Institute for Integrative Cancer Research, Massachusetts Institute of Technology, Cambridge, MA 02139, United States

Contents

Design concept

Our synchro-excited free-running (SEFR) method aims at efficient acquisition of high dynamic range SWIR photoluminescence kinetics from small volume liquid samples. Free-running acquisition with a Geiger mode (single-photon) detector is known to provide continuous detection of photons without extra waiting time (other than dead time for recovery),[1] and is considered the most efficient way to capture signals. However, conventional systems use periodic excitations that are asynchronous with free-running detections, so some emitted photons will arrive within the detector dead period. Also, excitations may occur while the detector is not blinded. This limits the measurement's dynamic range if the sample has strong prompt fluorescence, because the intense prompt emission will dominate the avalanche events and greatly reduce the opportunity for detecting delayed emission.

Exciting the sample during detector dead periods can prevent this problem, and we achieve this in our design by using detector pulses as the sole time reference. All operations are sequenced relative to those APD pulses and the timing origin is reset to zero every time the detector generates a pulse and begins its dead period. If the duration of that dead period is set to 27 µs, the laser excitation can be triggered to occur between 26 and 27 µs. Strong sub-microsecond luminescence from the sample is then hidden inside the dead period and the weak delayed emission will be captured when the detector becomes active at the 27 µs mark. Therefore, SEFR acquisition embraces advantages from both the traditional free-running and gated mode designs. In addition, the use of tightly focused detection optics not only optimizes collection efficiency but also gives the ability to probe local sample environments and observe single SWIR-fluorescent nanoparticles such as single-wall carbon nanotubes.

Optical components

As sketched schematically in Figure 3b, our samples were excited with a modular laser diode emitter mounted on a thermoelectrically cooled stage (held at 18 °C). Compatible light sources include TO-packaged diodes emitting at wavelengths ranging from 375 nm to 2000 nm, and emission could be switched between continuous and pulsed modes depending on the experiment. In this work, we used laser diodes to excite C_{70} at 462 nm, rose bengal at 520 nm, methylene blue at 660 nm, and SWCNTs at 638, 660, or 808 nm. Minimum pulse durations were around 20 ns, limited by our counter's time resolution. For most experiments we set a pulse duration of 0.25 to 2 µs to efficiently excite the sample. The excitation power was measured to be ca. 9 to 22 nJ per 110 ns pulse for the 462 nm laser diode. Excitation laser light was passed through a short-pass dielectric filter, a neutral density (ND) filter wheel set, an iris diaphragm and a hole mirror coupler before it was focused by an aspheric fused silica lens into the sample cell. Resulting sample photoluminescence was collected at 180° by the aspheric lens, reflected at the hole coupler, and then passed through another neutral density filter wheel and a spectral filter wheel set into a fiber collimator. This focused the photoluminescence light into the 105 µm core of an optical fiber

leading to the input port of either a free-running InGaAs APD Geiger-mode module (ID Quantique model ID220), or alternatively to a modular InGaAs spectrometer (BWTek Sol 1.7).

The short-pass filter blocked longer wavelength backgrounds from the laser diode and the ND filter wheel adjusted the excitation power. The iris diaphragm cleaned the laser spatial profile and helped in achieving reproducible alignment. The hole coupler was a protected silver mirror on a fused silica substrate with a central 2 mm hole drilled 45° from normal. The excitation laser beam was aligned to pass cleanly through the hole. This design greatly reduces backgrounds, from several thousand with a typical dichroic beam coupler to only ~550 Hz, which is near the detector dark level. The aspheric fused silica lens gave minimal background luminescence. Because the limited aperture of the detector restricts the collection cone (max NA~0.22), the high NA lens does not increase the emission collection efficiency. However, it does minimize the required pulse energy. The estimated pulsed power density of the beam at its waist is ~310 kW cm^{-2}, corresponding to an average power density of only 34 mW cm^{-2}. Our lens had a back focal length of 4.53 mm, allowing samples to be held in standard 10 mm path length cuvettes. A benefit of the tight excitation focusing is enabling measurements on single nanoparticles in dilute solutions.

By adjusting the ND filters in the emission path, we could extend the detection dynamic range to measure both prompt and delayed luminescence components, which commonly differ in intensity by at least 3 orders of magnitude. The spectral filter wheel selected spectral regions centered at 1050, 1125, 1200, 1275, 1350, or 1425 nm with 50 nm band widths to give kinetic curves with coarse spectral resolution. The compact emission double filter wheel assembly, which includes neutral density and spectral filter wheels, was positioned in the 6 mm gap between the hole coupler and fiber collimator lens. We also attached a 5 mW 1310 nm injection diode laser onto a buffer-free section of the optical fiber. Strong optical pulses from this laser leaked into the fiber core to force triggering of the InGaAs APD in order to restart acquisition cycles and increase data acquisition efficiency.

Signal control and processing

The core concept of SEFR-SPC is synchronizing all operations to the output pulses of the free-running APD. Therefore, the APD pulses not only deliver the photon arrival information, but also serve as active triggers that reinitialize the acquisition timing sequence with each detection event. Operations such as laser excitation are timed relative to that reference.

Control circuitry

The control circuitry records the arrival times of APD output pulses and drives the lasers with pulse delays and widths set by the computer. Figure 3a shows the control circuit schematic diagram. There is one signal input (from APD pulses) and two outputs (for injection and excitation lasers). The whole unit is composed of a commercial 8-channel digital counter and two home-made laser driver circuits. The counter registers the APD pulses and triggers the laser diodes. Those trigger pulses are sent to the laser driver circuits to generate either continuous or pulsed excitation with

selectable optical power. The maximum drive current of ca. 3 A is limited by the choice of transistor in the driver circuit. Our circuit allows the excitation laser diode to produce more than 1 W of optical power without excessive heating of the emitter. The time resolution of all operations, including measuring photon arrival time and setting laser pulse duration, is limited by the maximum timer frequency, which is 48 MHz (20.08 ns period).

Here, we show the detailed connections and components. The commercial 8-channel counter is the only module used for timing processing and triggering. Because all events are referenced to APD output signals, no external master controller is required. Figure S1a shows the connections on the counter unit. The slave components including excitation laser and injection laser are set for specific delays and pulse durations after every APD pulse, but their emissions must be capable of being stopped at unpredictable times. Therefore, each slave component requires two channels with an AND gate to allow pulse truncation. The internal timer (maximum 48 MHz clock frequency) was sent to the counter inputs (C1I - C5I). The APD signals were sent to C0I for counting and to counter gates (C2GT - C5GT) for resetting the counter time. Figure S1b shows the home-made circuit used for driving the injection laser. The output of the AND gate was pulled-up by a 5V voltage regulator and the voltage level can be adjusted using the potentiometer. The optical power of the 5 mW 1310 nm laser diode was tuned to 5 mW, as measured by a calibrated power meter. Figure S1c shows the driving circuit of the excitation laser. To achieve sharp edges for laser switching and tunable power levels, the circuit uses three transistors. The potentiometer on the second transistor (R6) was used to control the power of the excitation laser. Usually, tuning of the power level is required when switching between continuous and pulsed modes or when switching to a different laser diode. The third transistor can provide currents up to 3 A and the 12 V power supply gives enough voltage to drive shorter wavelength laser diodes.

Interval sequence

The only kinetic information recorded from this system is the interval sequence, which is a list of all time intervals between successive detector output pulses. To illustrate, the pulse train in Figure 2 represents the free-running APD pulses. The values $\tau_1, \tau_2, \tau_3 \cdots$ are the intervals between adjacent APD pulses (see Figure 2). As described above, all the times for operations are pre-set and referenced to the APD pulses. Therefore, it is not necessary to record any other sequence data. Our counter measures intervals between APD pulses by counting timer clock cycles (at its highest clock frequency of 48 MHz) during a gate that is toggled by APD pulses. The timing data are read out at a fixed rate of 480 kHz, with each value being an integer between 0 and 100. Values of 100 (gate ON) and 0 (gate OFF) both represent a duration of 2.08 µs, and any number between 100 and 0 (gate switching) represents that percentage of the 2.08 µs clock period. The counter is reset to zero after each readout. Figure S2 shows a detailed chart of the pulse counting and interval sequence conversion. In this way, every time interval between detector output pulses is saved as a number of counter ticks, which are easily converted to time units using the known clock frequency. Note that the number of entries equals the total number of APD pulses and that total acquisition time is the sum of all tick values divided by clock frequency. This format encodes the complete

set of luminescence kinetic data in a compact and simple form. In our instrument, we prefer to record the interval sequence as ticks plus counter frequency because the tick numbers can be saved as unsigned 16-bit integers that occupy only half the memory that would be required to save intervals as double-precision time values. It is worth mentioning that in the traditional first-in-first-out (FIFO) acquisition mechanism, both input signals (excitation) and output signals (APD pulses) need to be recorded. This requires much more sophisticated time tagging electronics. In comparison, our method records only output signals because input signals are synchronized to the output signals. Therefore, only a single time sequence is required.

Pulsed mode excitation

This instrument is intended for studies of relatively long-lived excited states, so sub-microsecond excitation pulses are sufficiently short. We generate laser diode pulses with selectable durations as short as 20 ns. Two excitation schemes are used. In Type 1 (Figure 2a), pulses are timed to be entirely within the detector's dead period, whereas in Type 2 (Figure 2b) they extend beyond the detector's dead period. Type 1 excitation can be controlled from a digital delay/pulse generator. The advantage of such dead period excitation is to shield the detector from large emission signals from a sample's fast-decaying luminescence, such as intense fluorescence. Otherwise, the strong prompt luminescence would consume most of the APD detection probability and greatly reduce the detection efficiency for weaker, slow components. The high count rate could also lead to distortions such as higher backgrounds. Therefore, to detect delayed fluorescence from samples such as SWCNTs, Type 1 excitation is necessary. By contrast, in Type 2 excitation the sample is excited while the detector is active. Type 2 excitation can also be tuned to a desired start time and duration, but must be terminated when the next detector pulse arrives. The excitation might then be totally passed in a cycle if the next detector pulse arrives before the trigger time of the excitation pulse. This type of setting ensures proper initialization of every detection cycle, in which the APD detector has the full 27 µs dead time to recover. Because excitation pulses might need to be terminated early, Type 2 excitation cannot be simply implemented using a delay generator. We will describe below how to combine Types 1 and 2 excitation modes to extend the acquisition dynamic range up to ~8 orders of magnitude.

Forced triggering

Because collection cycles are initiated by APD output pulses, which may occur at rates as low as the ~500 Hz background level, data acquisition efficiency could be very low. Data collection is accelerated for stronger emission signals, but then complications may occur, including nonlinear effects in the sample and detector saturation. To increase data acquisition efficiency without such complications, we introduce the technique of forced triggering. This is achieved by injecting pulses from an external 1310 nm laser (5 mW) directly through the wall of the optical fiber into the APD detector (Figure 3b). This induces a prompt output pulse and starts a new acquisition cycle. As shown in Figure 3a, the triggering laser diode is controlled by the injection laser circuit. The pulse timing configuration is the same as for excitation laser control except the Laser OFF time is set to

infinity to ensure that the injection laser will be kept ON until the APD senses a photon. If detection occurs before the trigger delay, t_w, triggering is skipped for that cycle. Figures 2 illustrate the timing sequence for the injection laser with respect to the APD pulses. Most of the forced triggering pulses induce an APD detector output pulse within 30 µs. The circuit for controlling the triggering laser is diagrammed in Figure S1c, and Figures S3a and S3b plot background and $^1O_2$ luminescence decay measurements with various trigger delay values, t_w (active time windows).

Figure S3a shows that the fitted background accurately models background signals for a wide range of t_w values, while noise is reduced as t_w decreases. This demonstrates the presence of a universal background, independent of t_w. That background is sensitive only to static properties of the APD detector such as applied voltage, so we measured a characteristic background function for each of the three detector efficiency settings. Also, because the power of the injection laser was fixed, the count rate from the injection laser should be constant, near 5×10^5 photons per second, as shown in the figure.

Figure S3b displays measurements of $^1O_2$ photoluminescence decay photosensitized by C_{70} in toluene, using various t_w values. The results show expected pure exponential decays, with the intensities and shapes independent of trigger delay, except at the 50 µs setting. In that case the small t_w value shifts intensities higher because of charge accumulation from photons in previous cycles. Therefore, it is important to set t_w to a value several times greater than the luminescence decay constant so that it will not cause an artificial intensity shift and shape distortion. Even so, some residual emission photons may still be collected when the dead period is not much longer than the emission time constant. One can then correct the data by deleting events i with values of τ_{t-1} that are too short. The constant count rate of the injection laser provides a good reference for the intensity of kinetic curves when absolute values are not available.

As described in the above, forced triggering of the detector accelerates the signal acquisition rate by reducing unwanted waiting time. Because the synchronized excitation-detection in SEFR mode fixes the time between excitation and forced triggering within each cycle, we expect that backgrounds and detected signals should not depend on changes to the acquisition time or the forced trigger delay. As a check, Figure S3 displays measurements of the backgrounds and signals with and without forced triggering. The results show that all backgrounds are the same without forced triggering as for forced trigger delays (active time windows) of 20, 100, 200, or 400 µs. We demonstrated that the intrinsic backgrounds are consistent and predictable so that they could be subtracted in the correction protocol. We also demonstrate in Figure S3b that measurements of signals such as singlet oxygen luminescence are consistent when using different active time windows. The signal could possibly be distorted only when the active time window is so short that residual signals from previous cycles could accumulate. This is a general problem in time domain acquisition.

Kinetic curve and multi-step correction protocol

To convert interval sequence data into a kinetic plot, one sorts the intervals into a histogram with uniform time bins. No extra timing data on correlations between excitation and detection are needed. We have developed a six-step correction protocol to recover accurate results for emission intensities *vs.* time and wavelength (Figure S4). These corrections, especially for the pile-up effect, are possible because of the complete time record of detection events (from zero to infinity) and the fixed time between detection and excitation for each cycle. The first five corrections are universal, in the sense that their correction parameters are fixed when the same detector, detector temperature, and detector applied voltage are used. Parameters for these corrections thus need to be carefully determined only once, after which they can be permanently incorporated into the data reduction software. The last correction, number 6, is settings-dependent, so it needs to be measured after each change in parameters such as excitation pulse duration.

Correction 1: Pile-up effect

For a Geiger mode counter, the time histogram of photon counts from a luminescing sample can be distorted because only one photon is registered per excitation cycle, so any subsequent photon events in the cycle are not counted. This kinetic distortion, termed the pile-up effect, may be described using statistical survival analysis. The probability density $f(t)$ for detecting a photon in time interval $[t, t + dt]$ equals the product of the sample's true kinetic probability function $K(t)$ and the survival probability function $S(t)$, which are assumed independent of each other. If a photon is detected before time t in a cycle, the detector will not detect other photons at or after that time. Therefore, the survival probability for the detector remaining active must decrease over time. Let $N(t)$ represent the measured number of detected photons in interval $[t, t + dt]$ summed over the many cycles of an experiment. The pile-up distortion can be treated using statistical survival analysis. Let the survival function $S(t)$ represent the probability that the APD shows no photon detection events until after time t. $S(t)$ equals one minus the sum of all event probabilities before time t, or the sum of all event probabilities after time t. The survival function is usually expressed in terms of $f(t)$, the time dependent event probability density function. The probability of detecting a photon in time interval $[t, t + dt]$ is $f(t)dt$ and

$$S(t) = \int_t^\infty f(\tau)d\tau$$

If we let $N(t)$ represent the total number of detected photons in interval $[t, t + dt]$ summed over the many cycles of an experiment, the probability density function and survival function can be rewritten as

$$f(t) = \frac{N(t)}{\int_0^\infty N(\tau)d\tau}; \; S(t) = \frac{\int_t^\infty N(\tau)d\tau}{\int_0^\infty N(\tau)d\tau}$$

We use $K(t)$ to represent the true kinetic function, which is the probability of detector counts with a constant survival function (the undistorted experimental result, as achieved in the limit of low excitation intensity). Because each measurement cycle is independent from the others, the survival function and the true kinetic function should be independent. Therefore, the probability of detecting a photon is the product of survival function and the true kinetics function, or $f(t) = K(t)S(t)$.

Then

$$K(t) = \frac{f(t)}{S(t)} = \frac{N(t)}{\int_t^\infty N(\tau)d\tau} \tag{1}$$

Provided that t_w, the detector time until forced triggering, is chosen much greater than the characteristic sample decay time, this equation allows accurate extraction of the proper kinetic function from raw data distorted by the pile-up effect. This shows that the pile-up effect can be corrected only if events at all times after t are recorded. This is true for our SEFR mode acquisition because the detector active period is not terminated by the next excitation pulse. Instead, the next excitation pulse is synchronized to detection.

The time bin of our histogram is channel width Δt_{ch}, equal to the electronic timer resolution. We can then express the pile-up corrected count rate in discrete form as

$$I_t = \nu K(t) = \nu \frac{n_{ch,t}}{\sum_{i>t}^\infty n_{ch,t}} \tag{2}$$

where I_t is the instantaneous count rate in time channel t, ν is the counter frequency, and $n_{ch,i}$ is the total number of counts recorded in channel i. Figure 1a shows a kinetic histogram found from interval sequence data that were measured with steady illumination and the time window parameter t_w set to infinity. The first 27 µs shows no signal because the detector was in its dead period following a detected event. After 27 µs, there is apparent near-exponential decay despite the actually constant photon flux. This reflects the pile-up distortion effect of a Geiger-mode detector, as discussed above. Figure 1b shows the kinetic histogram deduced from the same data after pile-up correction using eq. 2. This result properly indicates a near-constant count rate at times beyond 27 µs, with a value correctly matching the averaged count rate. The slight remaining distortion is due to effects from detector background, detector temporal sensitivity, and instrument response, which are discussed below. To illustrate with examples, we first rearrange the equation to obtain

$$\frac{N(t)}{K(t)} - \int_t^\infty N(\tau)d\tau = 0$$

Taking the derivative of the above equation gives

$$\frac{d}{dt}\left(\frac{N(t)}{K(t)}\right) - [-N(t)] = 0$$

$$\frac{1}{K}\frac{dN}{dt} - \frac{N}{K^2}\frac{dK}{dt} + N = 0$$

$$\frac{dN}{dt} + N\left(K - \frac{1}{K}\frac{dK}{dt}\right) = 0$$

or

$$N' + g(t)N = 0$$

where $g(t) = K - K'/K$. A general solution could be found to have the following form

$$N(t,c) = ce^{-G(t)}$$

where c is an arbitrary constant and $G(t)$ represents antiderivatives of $g(t)$, that is

$$G(t) = \int_0^t g(u)du$$

Therefore, only limited types of functions can be analytically solved.

Example 1: $K(t) = constant = K_0$,

$$g(u) = K_0$$

Hence

$$N(t,c) = ce^{-K_0 t}$$

Therefore, the measured count rate with the Geiger mode detector would be a single exponential decay and higher photon rate would give a shorter apparent decay time constant. This result matches our observation shown in Figure 1, and it matches the reported function derived from Poisson statistics assumption.[2]

Example 2: $K(t) = K_0 e^{-kt}$,

$$g(u) = K_0 e^{-ku} - \left(-\frac{kK_0 e^{-ku}}{K_0 e^{-ku}}\right) = K_0 e^{-ku} + k$$

$$G(t) = \int_0^t (K_0 e^{-ku} + k)du = kt - \frac{K_0}{k}(e^{-kt} - 1)$$

The measured count rate is

$$N(t,c) = c \cdot \exp\left[-kt + \frac{K_0}{k}(e^{-kt} - 1)\right] \tag{3}$$

This relation was tested with the singlet oxygen signal in Figure 4. We successfully fit the decay curve using the deduced function, obtaining an R-squared value of 0.9999. Eq 3 is also very similar

to the reported function derived from Poisson statistics except a small exponent difference of kt (Table S4).[2]

The two examples above show how the special cases of constant and exponential functions are distorted in predictable ways by the pile-up effect. Because SEFR acquisition can record detection event times from zero to infinity in each cycle, it offers the added benefit of allowing accurate pile-up correction for arbitrary decay functions. We also note that because of the ability to correct arbitrary curves, the SEFR-SPC allows accurate removal of dark and after-pulsing backgrounds, and temporal sensitivity, which are not simple constant or single exponential decay curves (see Figures S6 and S8). As described in the previous examples, researchers have discussed the corrections for constant and single exponential curves in 1974.[2] The predicted distortion for constant and single exponential decay are the same as the results we obtained (except for the small kt difference for single exponential decay). However, there were several key differences in conventional TCSPC: 1) *The Poisson distribution was assumed.* The constant excitation intervals make this assumption always true. 2) *Large acquisition number and small detection probability in each channel are required.* These two requirements lead to inefficient acquisition for long kinetics. 3) *Only the distorted curves from constant and single exponential decay emission source can be expressed as analytic functions.* Point 3) applies to our SEFR-SPC as well.

Simulations in Figure S5 further illustrate the pile-up distortion effect for a range of signal intensities. We assume that the true incoming signal follows single exponential decay with a time constant of 100 µs and that the APD dead time is 27 µs. The incoming intensity parameter K_0 ranges from 1 to 100000. The black curve represents an extremely low signal, for which the measured curve correctly shows single exponential decay matching the incoming signal. However, as K_0 increases, the growing pile-up effect leads to a faster apparent decay and kinetic distortion.

Correction 2: Intrinsic backgrounds

The averaged background count rate of our InGaAs APD is around 500 Hz when its detection efficiency is set to 10%. However, the instantaneous background count rate varies with time relative to the APD pulses. As shown in Figure S6a, we measured dark backgrounds for different dead time settings from 5 to 27 µs. The after-pulsing effect gives an exponential decay that has fixed amplitude and time constant relative to the APD pulse. This after-pulsing is hidden when the dead time was set to longer values. In the present work, we fixed the dead time at 27 µs to suppress the high background at early times.

Besides the after-pulsing, dark counts also contribute to the background through the entire time range after the dead period. We could fit the time-dependent intrinsic backgrounds with the following empirical expression

$$\text{count rate}(t) = a + b\left[\frac{t - t_{\text{dead}}}{c + (t - t_{\text{dead}})}\right] + de^{-t/f} + ge^{-t/h} \tag{4}$$

where t is the time after the APD pulse and a, b, c, d, f, g, and h are parameters. As shown in Figure S6b, the instantaneous count rate is lower than the average (falling to 375 Hz) prior to 100 µs and then gradually increases with time. Even for the 27 µs dead time, a small decay feature appears from 27 to 50 µs, representing residual after-pulsing with a maximum amplitude of 100 Hz. The after-pulsing curves for 27 µs dead time could be fit with a mono-exponential decay for the 10% detector efficiency setting and with double exponential decays at the 15% and 20% settings (shown in Figure S7 and Table S1). The residuals between measured backgrounds and fitted curves confirm appropriate modeling. For a given detector, this correction curve will only be affected by the detector settings for dead time and efficiency. In other words, because the dark noise and after-pulsing are independent of external settings, the listed parameters can be incorporated into a LabVIEW program to automatically subtract backgrounds after every measurement.

Correction 3: Temporal sensitivity

The sensitivity of the detector is not constant over time. We tried to define and measure temporal sensitivity to correct for this nonideality. Signals were measured using a cw, constant power 808 nm laser illuminating a scatter plate placed at the sample position to direct some light into the detector. Our injection laser was disabled for this measurement. The averaged count rate was controlled at ~23 kHz. Figure S8 shows the count rate *vs.* the time after the end of the detector dead period. We define the temporal sensitivity function as the instantaneous count rate curve divided by the average count rate. Here, the temporal sensitivity equals one at 15 µs but changes dramatically at times prior to 1 µs, revealing the instability of correction in this range. The measured temporal sensitivity before 20 µs was smoothed for use as numerical correction data. For times after 20 µs, we fitted the temporal sensitivity by a polynomial curve to obtain an analytical expression. Note that the temporal sensitivity corrections were found to depend on detector efficiency settings. As shown in Figure S9, higher efficiency gives faster response. The temporal sensitivity rose to 90% at 1 µs with the efficiency set to 20%. Also, higher efficiency settings show more constant sensitivity over time. The temporal sensitivity correction should be applied to allow accurate kinetic measurements. The temporal sensitivity is also one of the universal corrections, so the sensitivity curves at all three detector efficiency settings were measured and incorporated into our LabVIEW program as permanent corrections.

Correction 4: Spectral response variations

The sensitivity of the InGaAs APD varies with wavelength over the SWIR region, so its quantum efficiency should be measured within the ranges of the spectral filters mounted in the filter wheel. Figure S10a shows the measurement setup we used for this. We found quantum efficiency as the measured detector count rate divided by the calibrated photon flux into the 105 µm optical fiber. That photon flux was from an irradiance-calibrated tungsten-halogen lamp attenuated by reflective ND filters with known optical densities. Two neutral density filters were used to attenuate the signal to a range of 10 – 20 k counts per second. Assume that the spectral power density of the

lamp at 1 m distance is $P(\lambda)$ (unit: W nm^{-1} cm^{-2}). After passing through two ND filters with transmittance of $T_3(\lambda)$ and $T_{1.3}(\lambda)$, the spectral power density becomes $P(\lambda)T_3(\lambda)T_{1.3}(\lambda)$. If the band pass filters have transmittance of $F_{\text{filter}}(\lambda)$, the light passing through all filters has the spectral power density $P(\lambda)T_3(\lambda)T_{1.3}(\lambda)F_{\text{filter}}(\lambda)$ at the fiber end. Because a photon detector was used, we convert the spectral power density into spectral photon flux by dividing power density by photon energy hc/λ, that is, $P(\lambda)T_3(\lambda)T_{1.3}(\lambda)F_{\text{filter}}(\lambda)\text{hc}/\lambda$ (units: photons nm^{-1} cm^{-2} sec^{-1}). Therefore, for each band-pass filter, the photon flux at the fiber end, which is the integrated spectral photon flux for each filter, becomes $\int[P(\lambda)T_3(\lambda)T_{1.3}(\lambda)F_{\text{filter}}(\lambda)\text{hc}/\lambda]\text{d}\lambda$ (unit: photons cm^{-2} sec^{-1}). We want to know the photon rate (photons/sec) at the fiber end, so the photon flux should be multiplied by the fiber area σ, to yield $\sigma\int[P(\lambda)T_3(\lambda)T_{1.3}(\lambda)F_{\text{filter}}(\lambda)\text{hc}/\lambda]\text{d}\lambda$ (unit: s^{-1}). The quantum efficiency is defined by dividing measured count rate **C** by the photon rate, which is

$$\frac{\mathbf{C}}{\sigma \int \left\{ P(\lambda)T_3(\lambda)T_{1.3}(\lambda)F_{filter}(\lambda)\frac{hc}{\lambda} \right\} d\lambda}$$

Measured values are plotted in Figure S10b and listed in Table S2. These parameters are also used for permanent corrections in our LabVIEW software.

As shown in Figure S10b, we found the quantum efficiency to be relatively flat over the SWIR range from 1000 nm to 1450 nm but sharply lower in the 925 nm range. Our measured quantum efficiency is only 55% to 60% of the value specified by the detector manufacturer. This discrepancy might reflect different measurement configurations and/or coupling losses into our fiber. We used our measured quantum efficiencies to convert count rate into photon flux incident on the fiber. These values provide insights into optical efficiencies when the absolute excitation power is known.

Correction 5: High dynamic range measurement

The InGaAs APD detector gives around 4 to 4.5 orders of magnitude of dynamic range. To prevent overloads when measuring the delayed luminescence of a strongly emissive sample, a neutral density (ND) filter with optical density of 3 (see Figure S11) was used to acquire the fast fluorescence component. The photon rate without the ND filter was then back-calculated using the filter's measured attenuation factor. Using this method, the dynamic range could be increased by 3 orders of magnitude on the high intensity side. In this study, we usually set the excitation pulse arrival at 32 µs (Type 2 excitation) when measuring a fast emission component with the ND filter, and at 26 µs (Type 1 excitation, 1 µs before end of dead period) without the ND filter. In post processing, the times of excitation were shifted to zero and then the two measured decay curves were merged together. The log-log plot of Figure S12 shows an example of measuring the instrument response function by this method using a sample, IR26, that has strong prompt fluorescence. Notice that there is a gap in photon rate of a factor of ~3 between the segments where count rate through the ND filter is too low but the time is too early for accurate tail measurements. Apart from this gap, the use of combined Type 1 and Type 2 excitations provides time-resolved

luminescence curves covering 8 orders of magnitude in intensity. Figure S11 shows the spectrum of the neutral density filter used for prompt luminescence measurement. The smoothed curve was incorporated into our LabVIEW program for Step 5 corrections.

Correction 6: Instrument response function

Photons incident on the detector during its dead period generate charges that accumulate and remain for a period. This phenomenon is sometimes called "charge persistence."[3,4] It results in an extra form of background in the instrument response function (IRF) at later times in the active window. This background level depends linearly on the intensity of light arriving within the dead period. Figure S12a shows a high dynamic range measurement of the IRF curve using an infrared dye, IR26, whose SWIR fluorescence lifetime is ~22 ps and has negligible emission on the nanosecond scale.[5] At 1 and 10 µs, the IRF shows photon rate factors lower than the peak by factors of ca. 3000 and 300,000, respectively. We also find that the IRF retains the same shape for a 100-fold change in excitation energy (Figure S12b), giving confidence in its accuracy. IRF correction of kinetic data is very important for samples with decay constants of a few microseconds or less. For example, measurement of SWCNT delayed fluorescence from triplet-triplet annihilation requires a dynamic range of seven orders of magnitude over the first 4 microseconds.[6] To obtain our standard IRF function, we smoothed the IRF data for the first ten microseconds and then spliced it onto an exponential decay function. The IRF becomes undetectably weak after 30 µs. Because it is highly dependent on the energy of the prompt luminescence, the IRF correction is the only setting-dependent correction in our correction protocol. We recommend re-measuring the IRF whenever there are changes to the excitation laser, dead time, excitation start time, or excitation duration.

Optional correction: Removing signals from previous excitation pulses

This correction might be required when the decay curves are much longer than the dead time. In this case, the sample luminescence does not have enough time to decay down to background level before the next excitation. The time intervals whose preceding intervals are too short then have to be removed from the data set. This may easily be accomplished after acquisition because the full sequence of intervals is available. This correction is most relevant for non-exponential decay functions.

Comparison of the optical efficiencies

To compare the optical efficiencies when the $^1O_2$ has different lifetimes, one can normalize the optical efficiency with the counts per cycle (total counts from time zero to infinity). Assume the time constant is τ and the decays are exponential

$$\int_0^\infty e^{-t/\tau} dt = \tau$$

Therefore, the ratio of the counts per cycle between two samples are τ_1/τ_2. The optical efficiency is defined as the emission intensity (I, unit: Hz) divided by the excitation power ($P_{ex.}$, unit: mW)

$$E_{optical} = \frac{I}{P_{ex.}}$$

The normalized optical efficiency then is

$$e_{optical} = \frac{E_{optical}}{\tau} = \frac{I}{\tau P_{ex.}}$$

The optical efficiency ratio between two instruments using different samples is

$$\text{ratio} = \frac{E_{optical,1}/\tau_1}{E_{optical,2}/\tau_2}$$

We measured optical efficiency with $^1O_2$ lifetime at 28.7 µs. The reported optical efficiencies with $^1O_2$ lifetime at 3.0 µs. The ratios of the optical efficiencies are

$$\text{ratio}_{APD} = \frac{3700/28.7}{350/3.0} = 1.1; \ \text{ratio}_{SNSPD} = \frac{3700/28.7}{3/3.0} = 129$$

The pile-up distortion

It has been shown that the pile-up distorted uncorrected data with decay constant τ_0 can be fit to a single exponential curve with time constant τ, where the relation between τ and τ_0 is[7,8]

$$\tau = \tau_0\left(1 - \frac{P}{2}\right)$$

Here P is the probability of detecting a photon in one cycle. To demonstrate this, we fit the raw data from Figure 4 using single exponential decay and obtained the fit result shown in Figure S20. The fitted time constant τ is 15.03 ± 0.02 µs and the true time constant τ_0 is 29.745 ± 0.007 µs. Putting our values into the formula gives

$$15.03 \pm 0.02 \text{ µs} = 29.745 \pm 0.007 \text{µs} \times \left(1 - \frac{P}{2}\right)$$

Then

$$P = 0.98$$

The apparent time constant is only half of the true time constant because of severe pile-up distortion. The distortion fits well to the ½ model (amplitude weighted mean), and the probability of detecting a photon P in a single cycle period is 0.98 (essentially 1), reconfirming the acquisition mechanism of SEFR-SPC.

The detection of one photon in each acquisition cycle implies that every acquisition cycle is meaningful. Experimentally, this requires high photon flux to the detector to create the condition. Otherwise, the detector will always be on if photon detections are missed. For example, the ~32 photon hits per excitation pulse shown in Figure 4 indicates severe pile-up distortion from multiple photon arrivals in an acquisition cycle. However, this severe pile-up distortion can be analytically corrected using eq 1. Our detection scheme shows an advantage when the kinetic curves are longer,

because the wait time for each cycle is much slower to acquire a complete profile. Some special methods have been reported to achieve multiple photon detection per cycle. Sergent et al. used a 2D detector to disperse the photons into different pixels.[9,10] Therefore, the authors could ensure that less than one photon hits a pixel per cycle, while all of the arrived photons could be detected and timed simultaneously. However, the disadvantage of this method is the limitation of the speed of a 2D detector, which is in the microsecond range.

The pile-up correction methods for TCSPC

Traditional TCSPC considers detecting one photon in channel i, and the probability can be written as

$$P_i = \frac{A_i}{M - \sum_{j=1}^{i-1} A_j}$$

where P_i is the probability of a photon event in channel i, M is the total number of photon events over all channels, and A_i is the number of events in channel i. Assume that the events follow a Poisson distribution. The real photon hit probability Q_i at channel i can be found as follows (Coates, 1968;1971):

$$Q_i = -\ln(1 - P_i)$$

Therefore, the number of photon hits N_i in a specific channel i after M detection cycles (sweeps) is

$$N_i = MQ_i = -M \times \ln\left(1 - \frac{A_i}{M - \sum_{j=1}^{i-1} A_j}\right)$$

Donodue and Stern[11] (1972) also showed identical results from another approach. The number of photon hits N_i is a function of the number of events in channel i and total detection cycles, $N_i = N_i(A_i, M)$. Even though the correction itself looks more complicated than eq 2, the pile-up can still be corrected, especially in gated mode detection. To reveal the difference between these two corrections, we used the raw data from Figure 4 and ran the corrections using eq 2 and equations above. The results are shown in Figure S21. It seems like the corrected curves from Survival Analysis and Poisson statistics are very similar, expect that a small offset is added to the Survival analysis model on the log scale. Note that this is a complex kinetic curve, combining single exponential decay in the first section and constant intensity in the second. Theories seem to have demonstrated the equivalence of these two models except for the constant.[12] For traditional asynchronous free-running detection, dead time can appear in the middle of detection cycles, hampering the consistency of detection probability. Therefore, the Poisson distribution requirement is not obeyed. Arrival of multiple photons within a detection cycle causes a nonlinear relation between true probability and measured probability. Meurs and van der Werf[13] (1976) attempted to remove the multiple photon events using a "pile-up inspector," which is a custom-built circuit to reject unwanted detection. Simulations also have been performed by Salthammer[14] (1992) to confirm the accuracy of the previously derived correction formula. In summary, the pile-up distortion from traditional TCSPC has been a critical issue for obtaining accurate kinetic curves.

The solution for it is generally to use high repetition rate and low photon flux, which works well for nanosecond range measurements. However, the acquisition of longer kinetic curves becomes inefficient because each acquisition cycle is significantly slower. SEFR-SPC provides an ideal solution for this case because it ensures that one photon can be detected in every cycle and that the resulting heavy pile-up distortion can be corrected accurately.
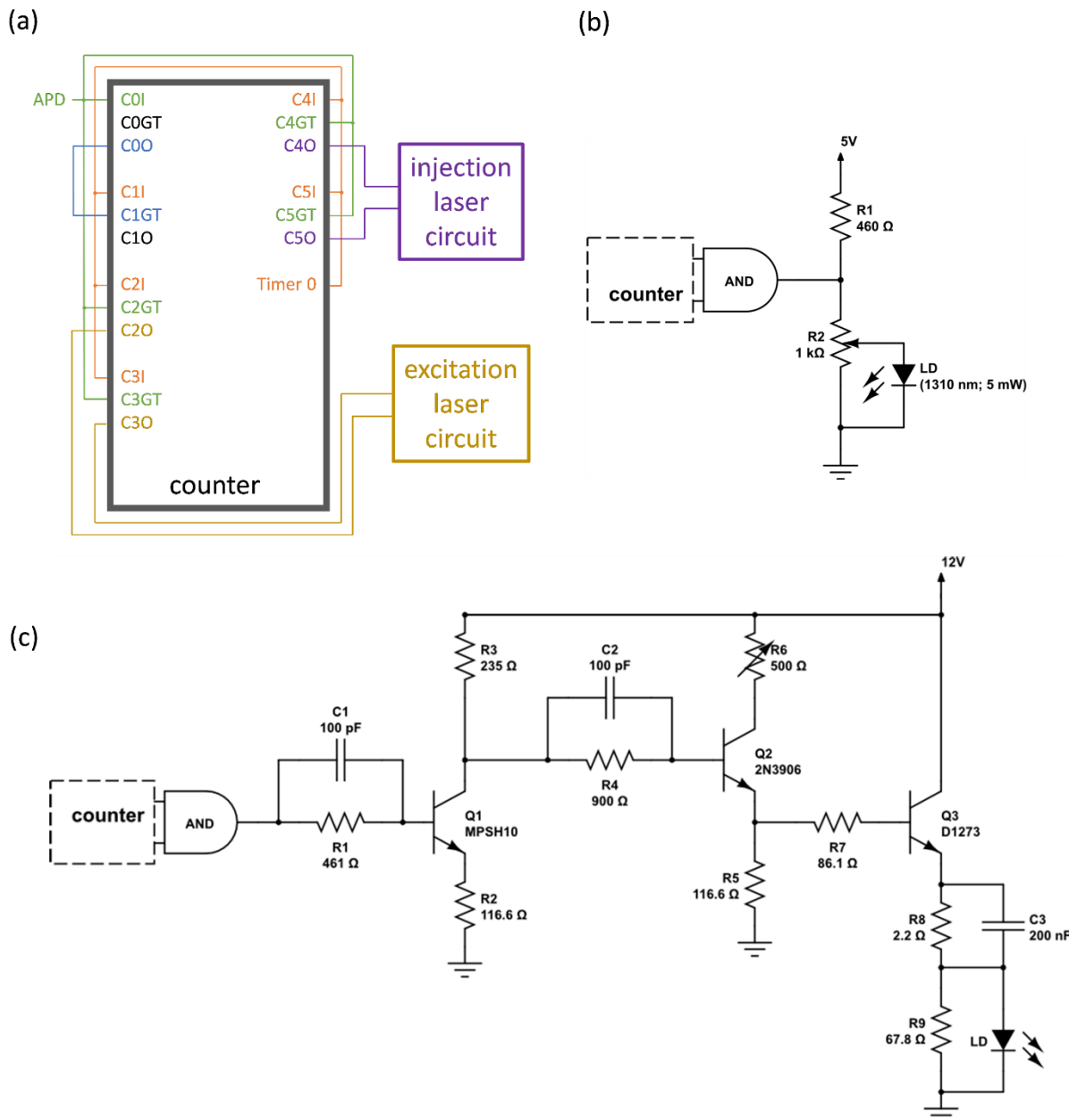
Additional Figures

(a)

(b)

(c)

Figure S1. Schematic diagram of the controller module. (a) Connections on the 8-channel counter. The only input is APD pulses and outputs are used to control the excitation and forced-trigger lasers. (b) Circuit for diode laser used for forced-triggering. A variable resistor was used to adjust the intensity of the laser. (c) Circuit design of the excitation laser. A variable resistor (R6) allows tuning the intensity of the laser. The excitation laser could be either pulsed or continuous mode.
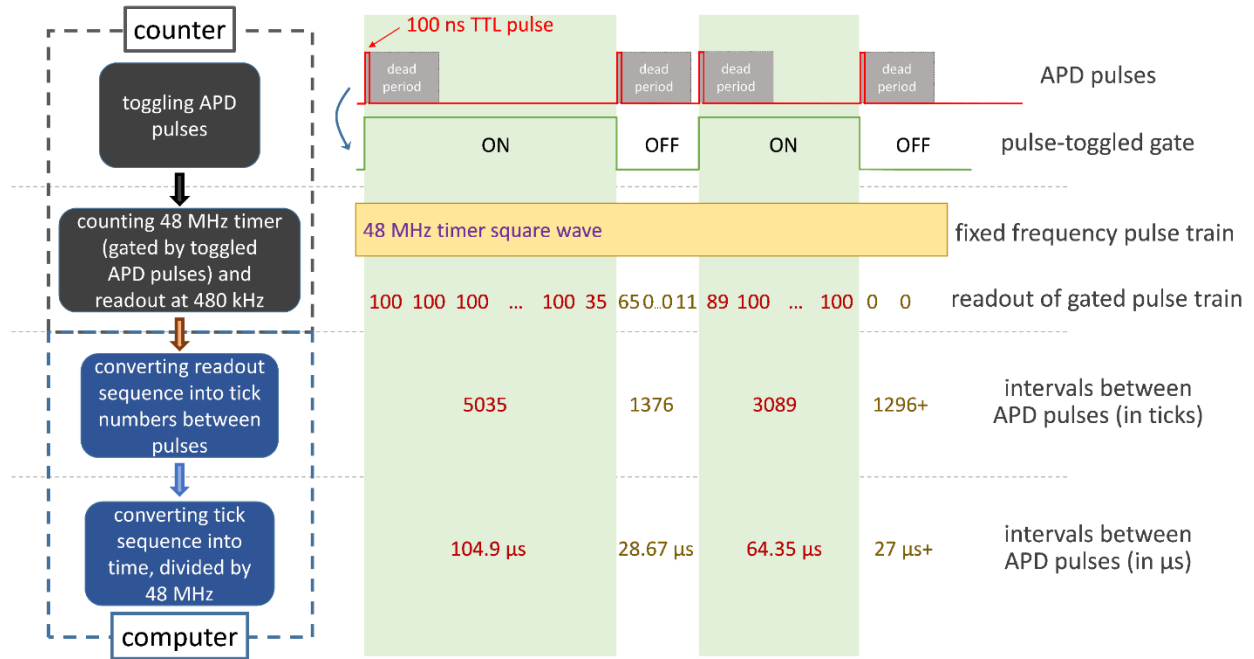
Figure S2. Method for measuring intervals between APD pulses. This procedure make use of two channels of the counter. The output of the first channel toggles when receiving 100 ns long photon detection pulses from the APD. The second channel counts the internal 48 MHz timer gated by the toggling signal train from the first channel. The counts of the timer pulses are read at a 480 kHz frequency and then cleared right after each readout. Therefore, the readout sequence shows a series of 100 when gate is on and a series of 0 when gate is off. The readout sequence is then sent to the computer and converted into the interval sequence in ticks, which is finally converted into the interval sequence in laboratory time.
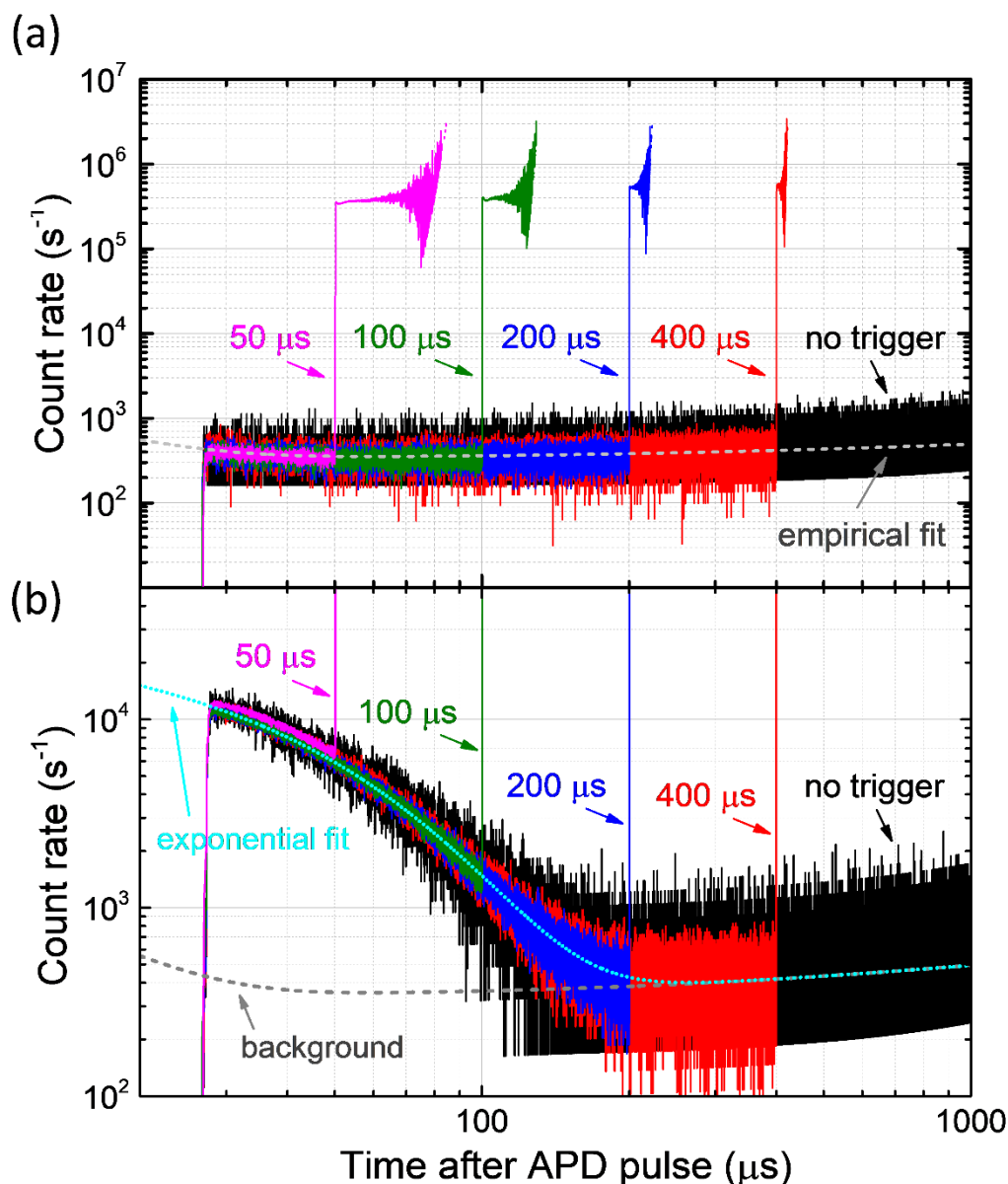
Figure S3. The injection laser restricts photon detection to a desired time window, t_w, by force-triggering the APD event. (a) Dark background measurement with various t_w values. Data are shown for the injection laser starting at delays of 50, 100, 200, 400 µs after an APD pulse, and also when it is not triggered. Results show a universal background curve at around 500 Hz count rate, which is independent of t_w. Curves with near constant count rates near 500 kHz represent the detected injection photons. The injection photons could force trigger an APD event within 40 µs. (b) Singlet oxygen luminescence at 1275 nm shows single exponential decay. Overlapped decay curves were observed with various t_w values, although the segment with 50 µs shows slightly higher values because at short t_w there is some accumulation of residual counts from the preceding pulse.
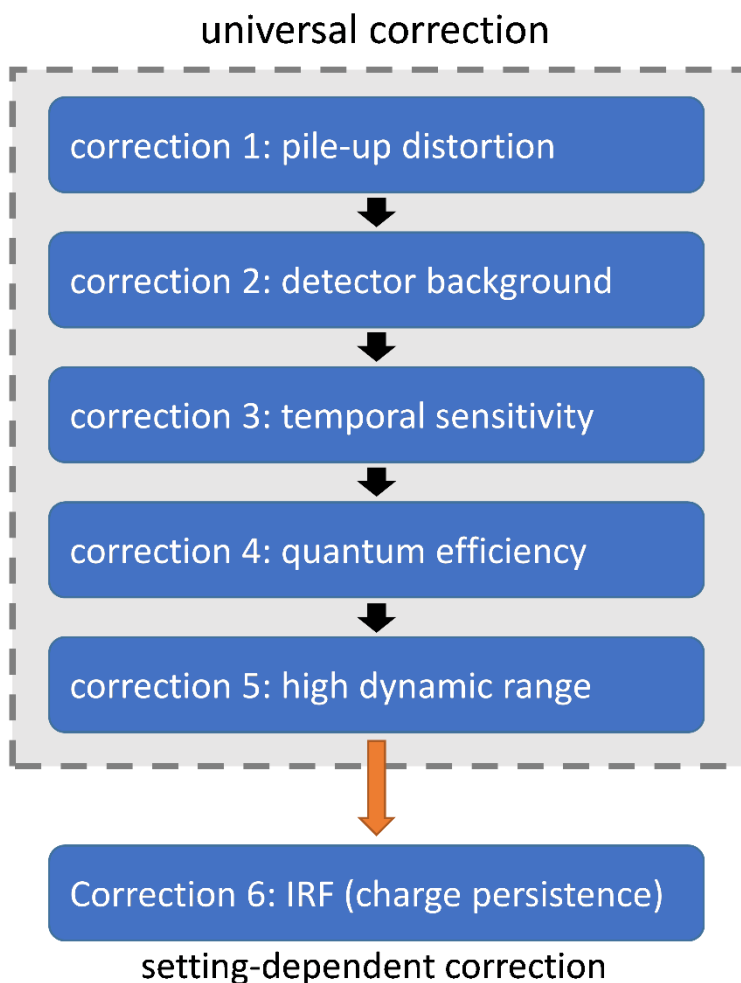
Figure S4. Suggested correction protocol. Corrections 1-5 are universal corrections that do not depend on instrument settings. Correction parameters should be carefully determined in the beginning and then applied permanently with the same detector and filters. Correction 6 is setting-dependent, and should be measured every time there is a change in excitation pulse duration or excitation source.
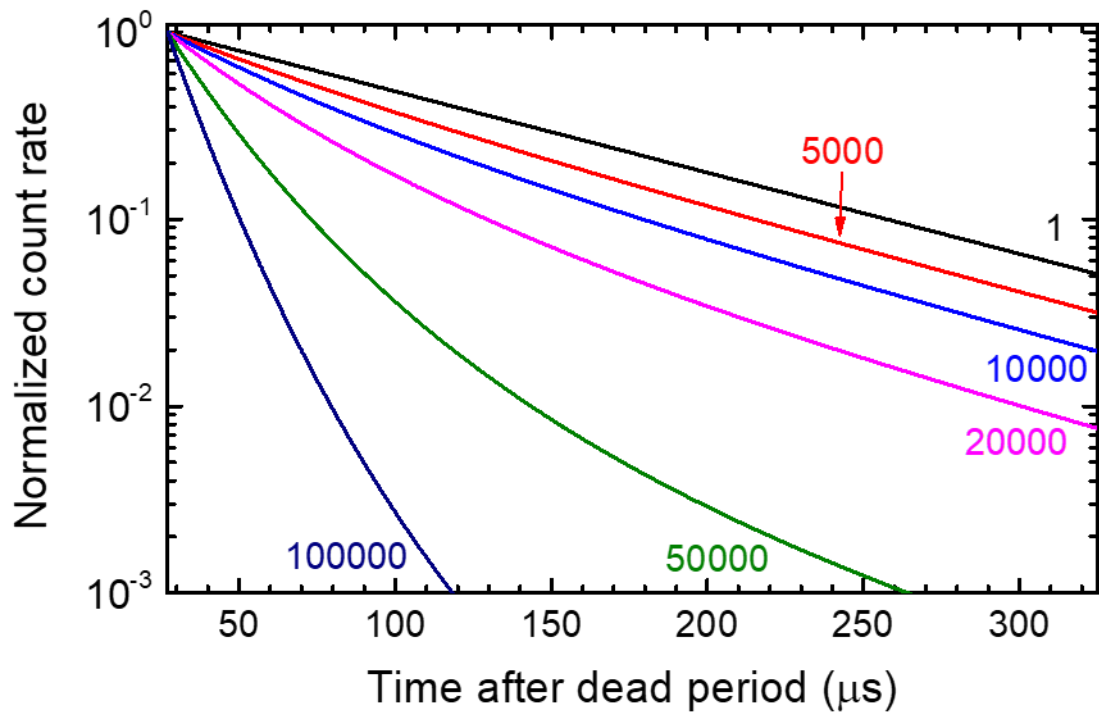
Figure S5. Simulation of pile-up effects on a single exponential decay signal. Numbers on the curves show relative intensities of the incoming signal. The curve labeled 1 gives the true sample decay kinetics. At higher intensities there are progressive distortions in apparent decay constant and shape. Detailed studies of the pile-up effect can be found in the literature, including various types of pile-up sources besides the detector.[13-23]
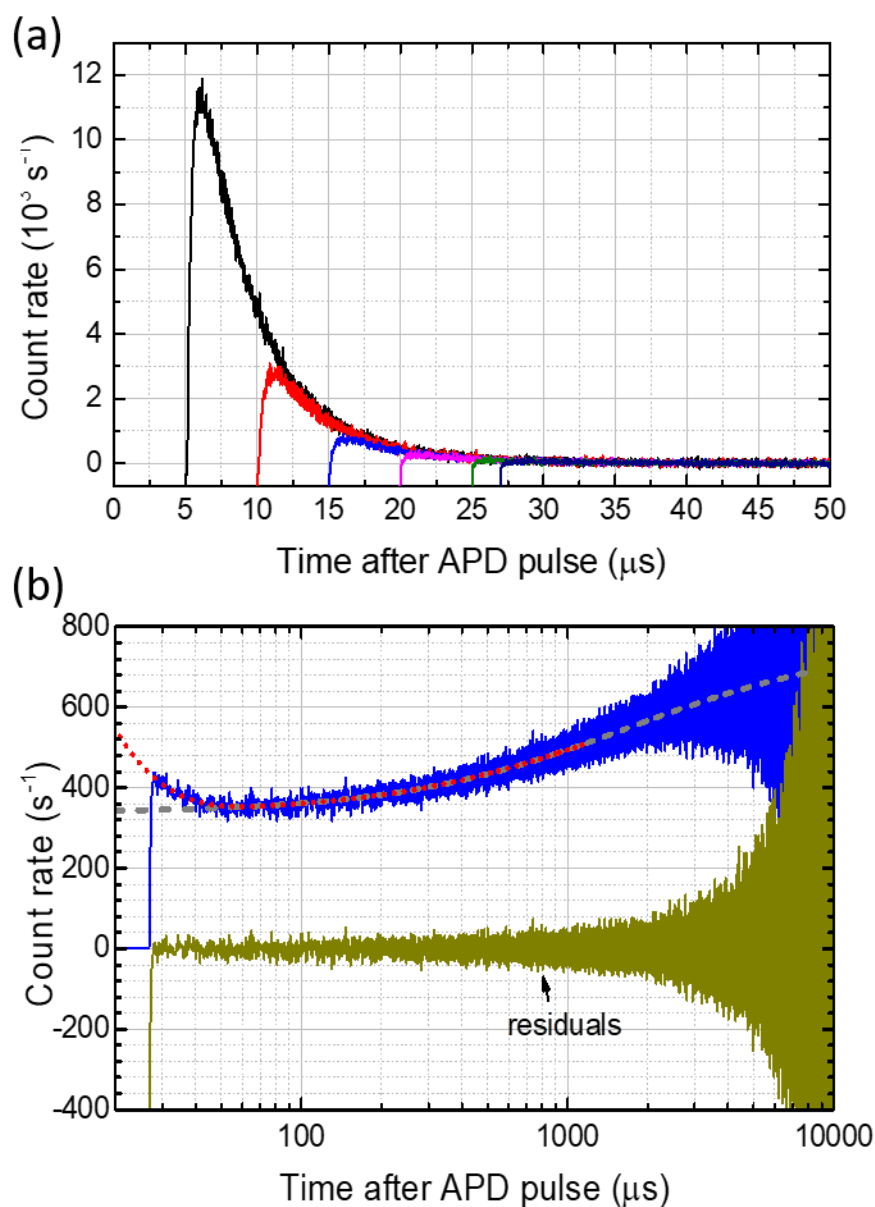
Figure S6. Removal of dark and after-pulsing backgrounds (Correction 2). (a) After-pulsing intensity is high at times close to the previous pulse (or when the dead time is short). Dead time duration has no effect on the after-pulsing curve, which is close to pure exponential decay. (b) Blue curve shows background measured in the dark for 5 hours. The instantaneous count rate increases gradually over time and could be fitted with the function $a + b(t - t_{dead})/(c + t - t_{dead})$, plotted as a dashed gray curve. The first 20 µs shows slightly higher background than expected, which could be explained as the residual tail of the after-pulsing and can be fitted as an exponential decay. The combined curve is plotted as the dotted red line. Residuals between measured and fitted backgrounds are shown in dark yellow.
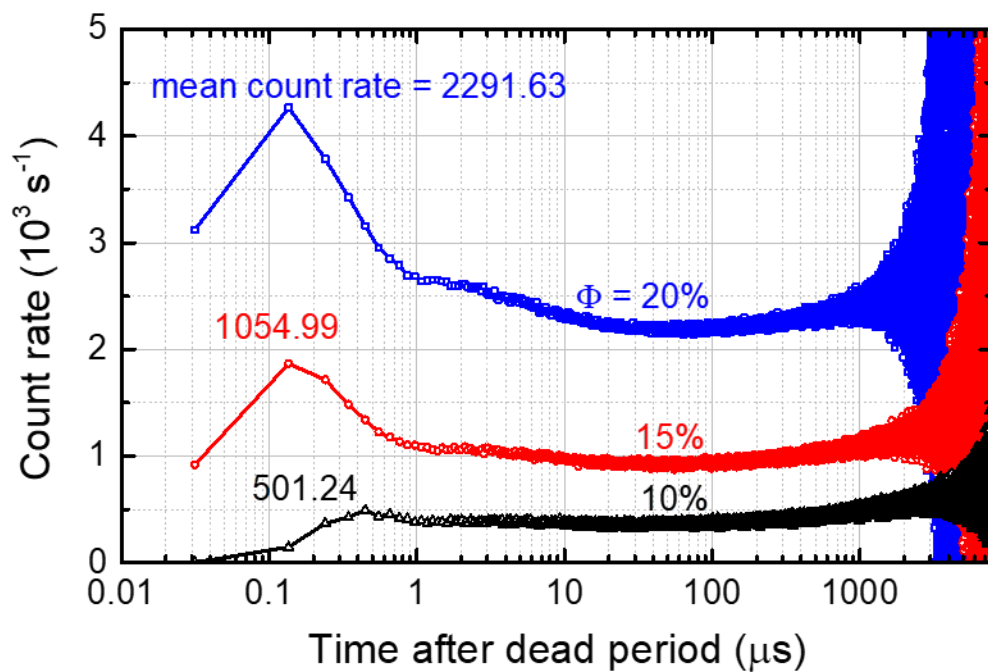
Figure S7. Backgrounds measured at different detector efficiency settings (10%, 15% and 20%). The averaged count rate increased nonlinearly with that setting.
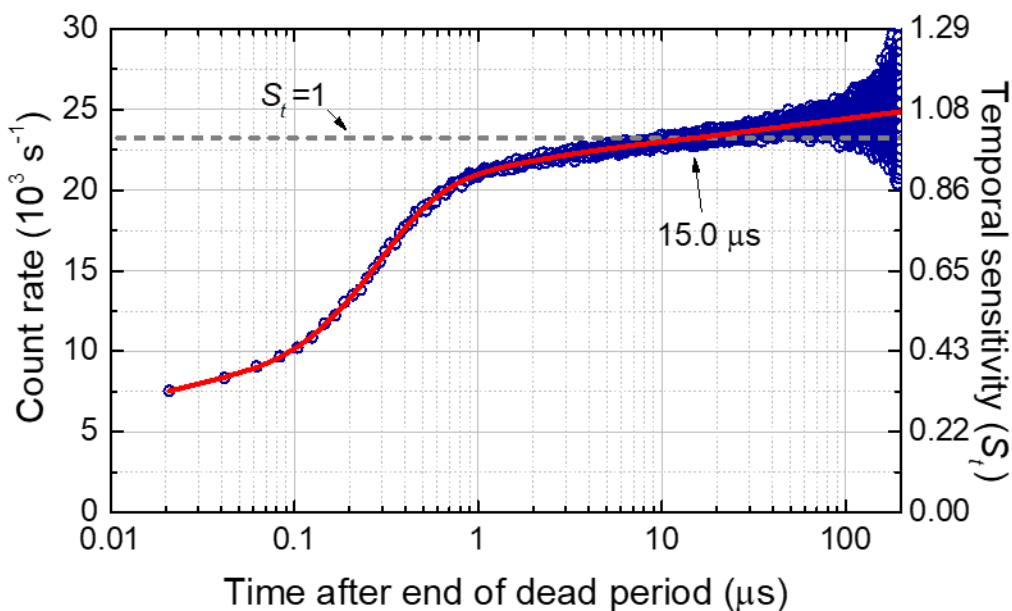
Figure S8. Temporal sensitivity (S_t) calibration measured with constant excitation light (Correction 3). Blue circles represent measurements with a constant light source. Temporal sensitivity is defined as instantaneous count rate normalized to averaged count rate (dashed gray). Red curve is the fitted curve for S_t correction. Instantaneous count rate at 15.7 µs is the same as averaged count rate. Therefore, the S_t is normalized to this point. The S_t increases over time within each cycle. The time before 1 µs is the rapid growth region and accurate calibration of the early S_t values is relatively difficult because the change is intensity dependent. However, calibration of sensitivity for times after 1 µs is consistent over wide range of incoming photon intensity.
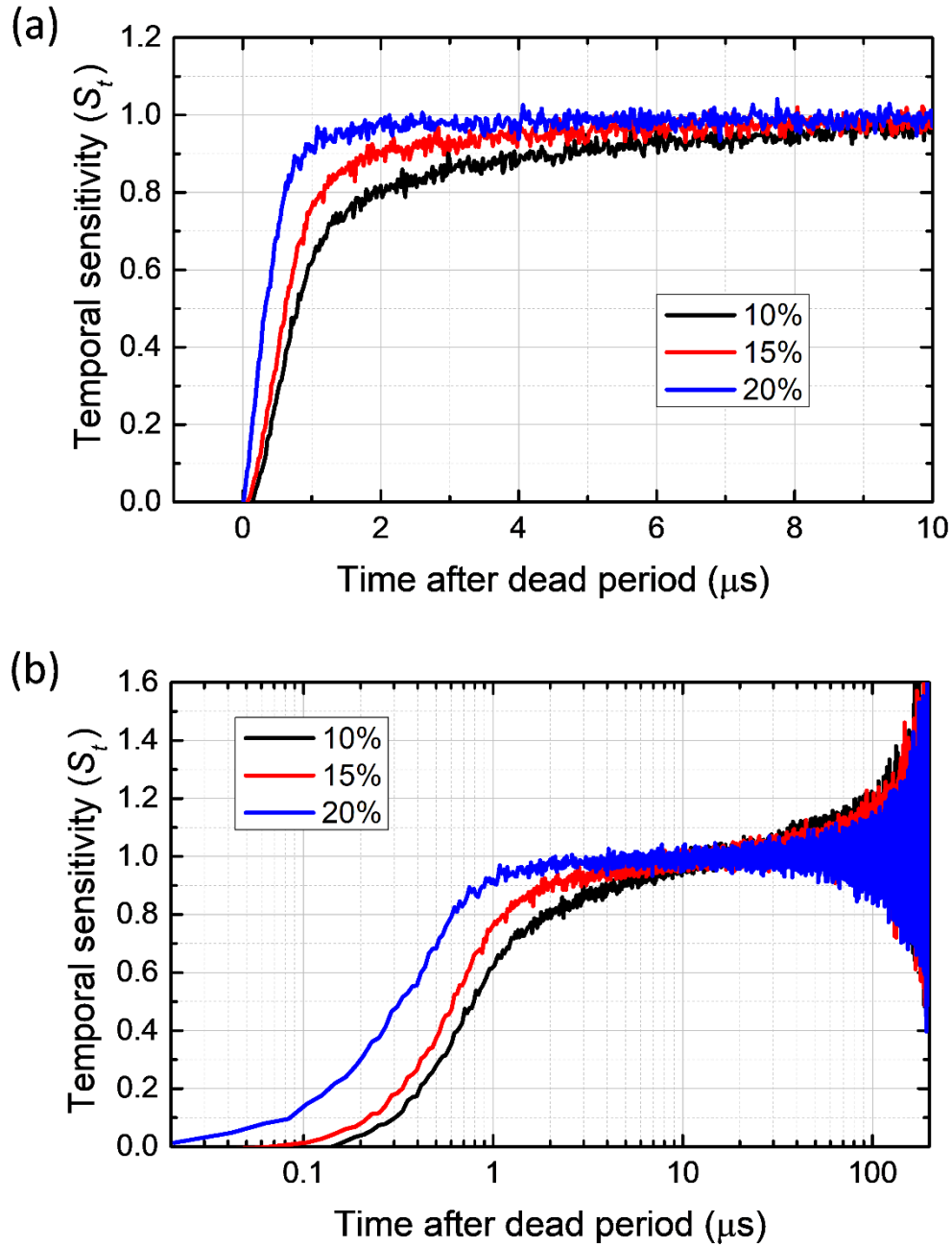
Figure S9. Comparison of temporal sensitivities at different detector efficiency settings. (a) detector temporal sensitivity for the first 10 µs after dead period. (b) temporal sensitivity over longer periods. The 20% efficiency setting shows a faster rising and flatter sensitivity function.
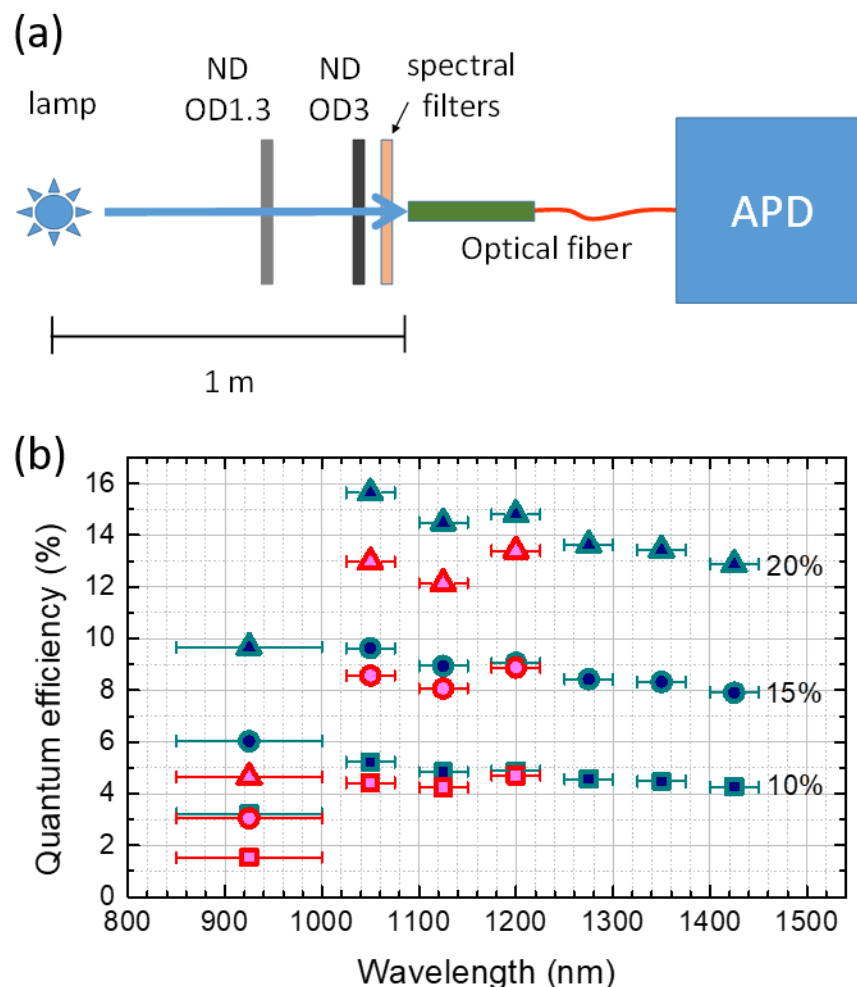
Figure S10. Measurement of detector quantum efficiency with various spectral filters (Correction 4) and nominal detector settings for quantum efficiency. (a) Optical setup used in the measurements, made based on flux at the optical fiber end. (b) Measured values. Data plotted in cyan color were measured without a 1300 nm short pass filter; data plotted in pink color were measured with a 1300 nm short-pass filter. Differences are mainly attributed to spurious transmission of the bandpass filters at wavelengths longer than 1400 nm.
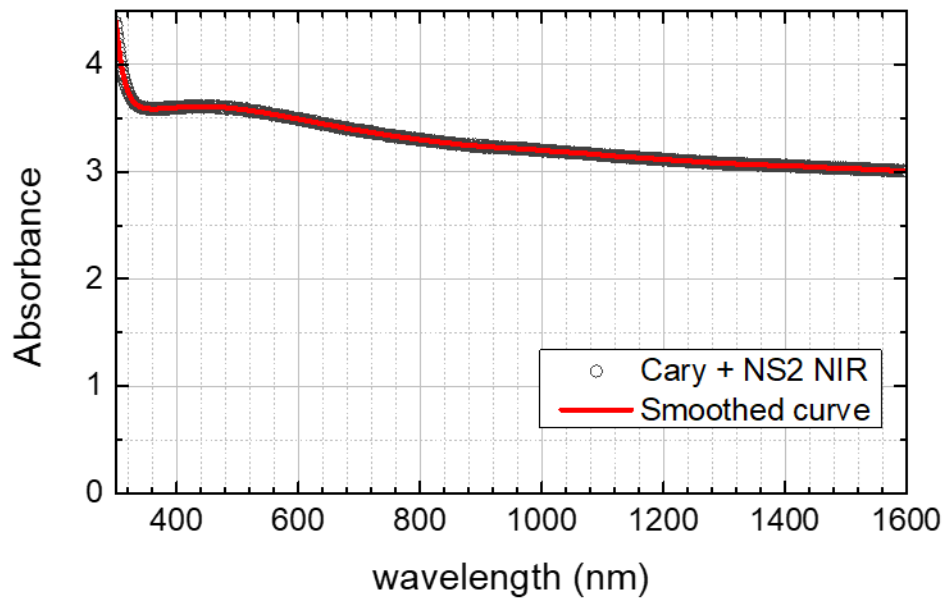
Figure S11. Absorbance of the neutral density filter placed in the emission path (correction 5). The filter was used when the excitation is triggered after the dead period to attenuate strong emission sample fluorescence by 3 orders of magnitude. This method extends our dynamic range up to 10^8.
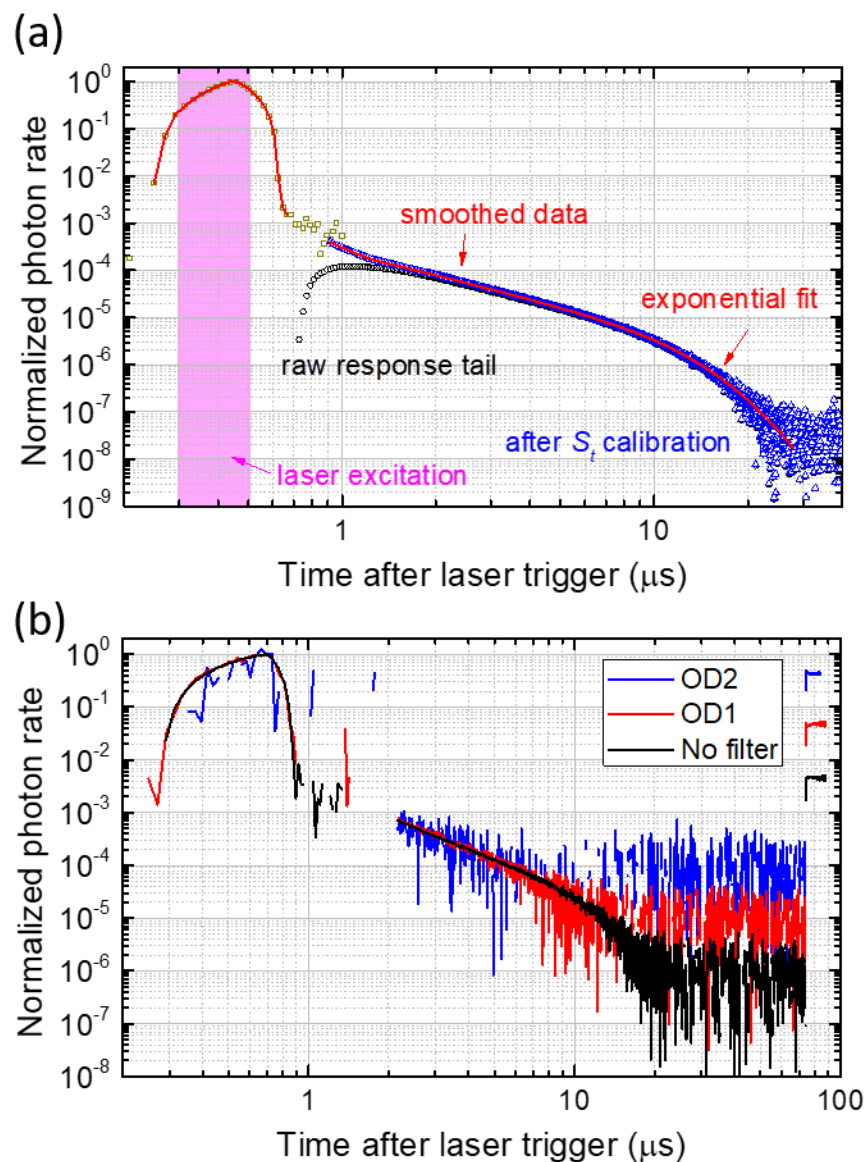
Figure S12. Instrument response function (IRF) measured with IR26 dye (Correction 6). (a) IRF using 808 nm laser diode with 250 ns pulse width for excitation. (b) IRF shows no significant intensity dependence using 3 different excitation powers spanning a factor of 100.
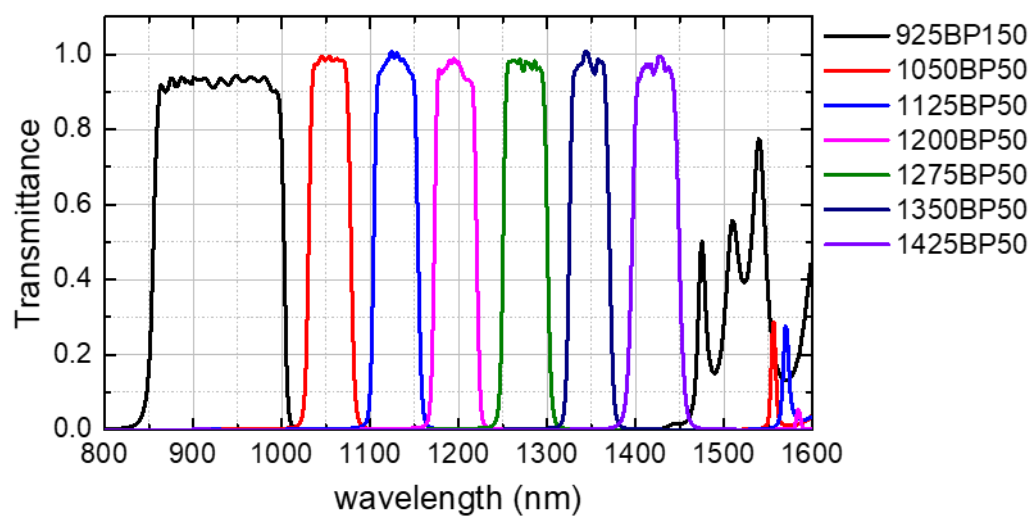
Figure S13. Transmission spectra of the filters installed in the emission filter wheel. Most of these filters have FWHM of 50 nm, except the 925 nm filter, which has a 150 nm band width. The first four filters have limited attenuation at wavelengths longer than 1400 nm.
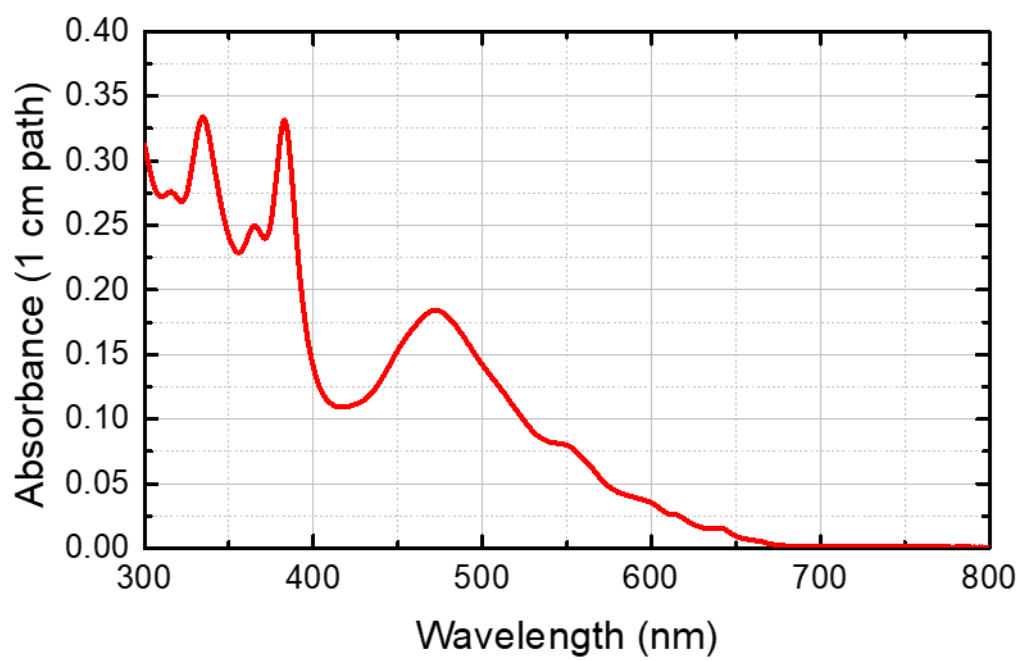
Figure S14. Absorption spectrum of C_{70} in toluene, used to sensitize singlet oxygen formation for the measurement in Figure 4.
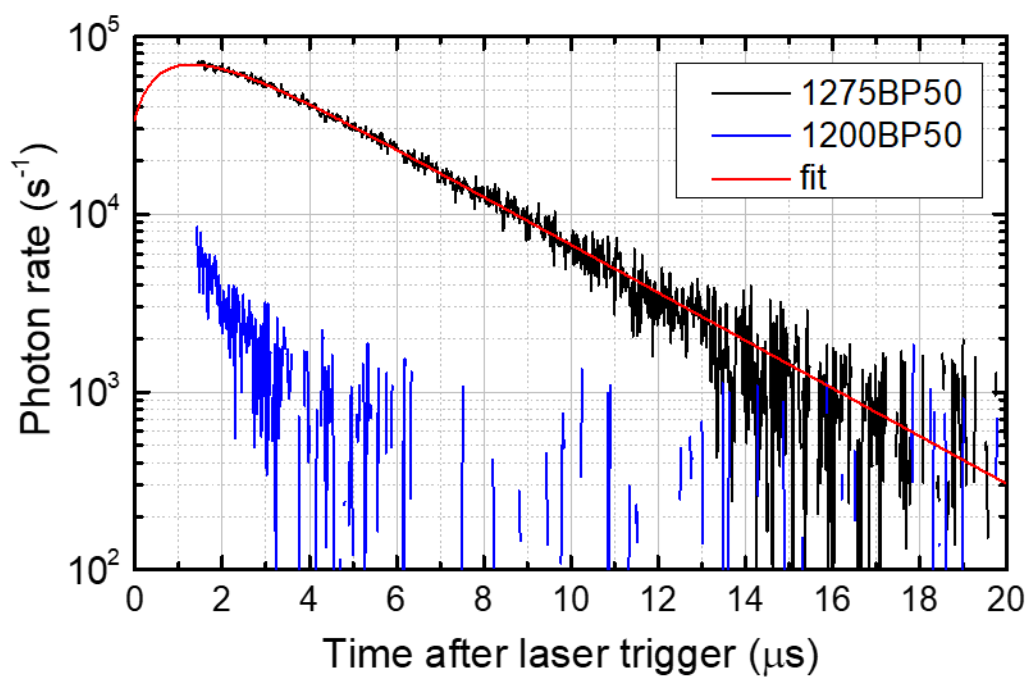
Figure S15. Singlet oxygen luminescence kinetics measurement in H_2O using rose bengal as photosensitizer.
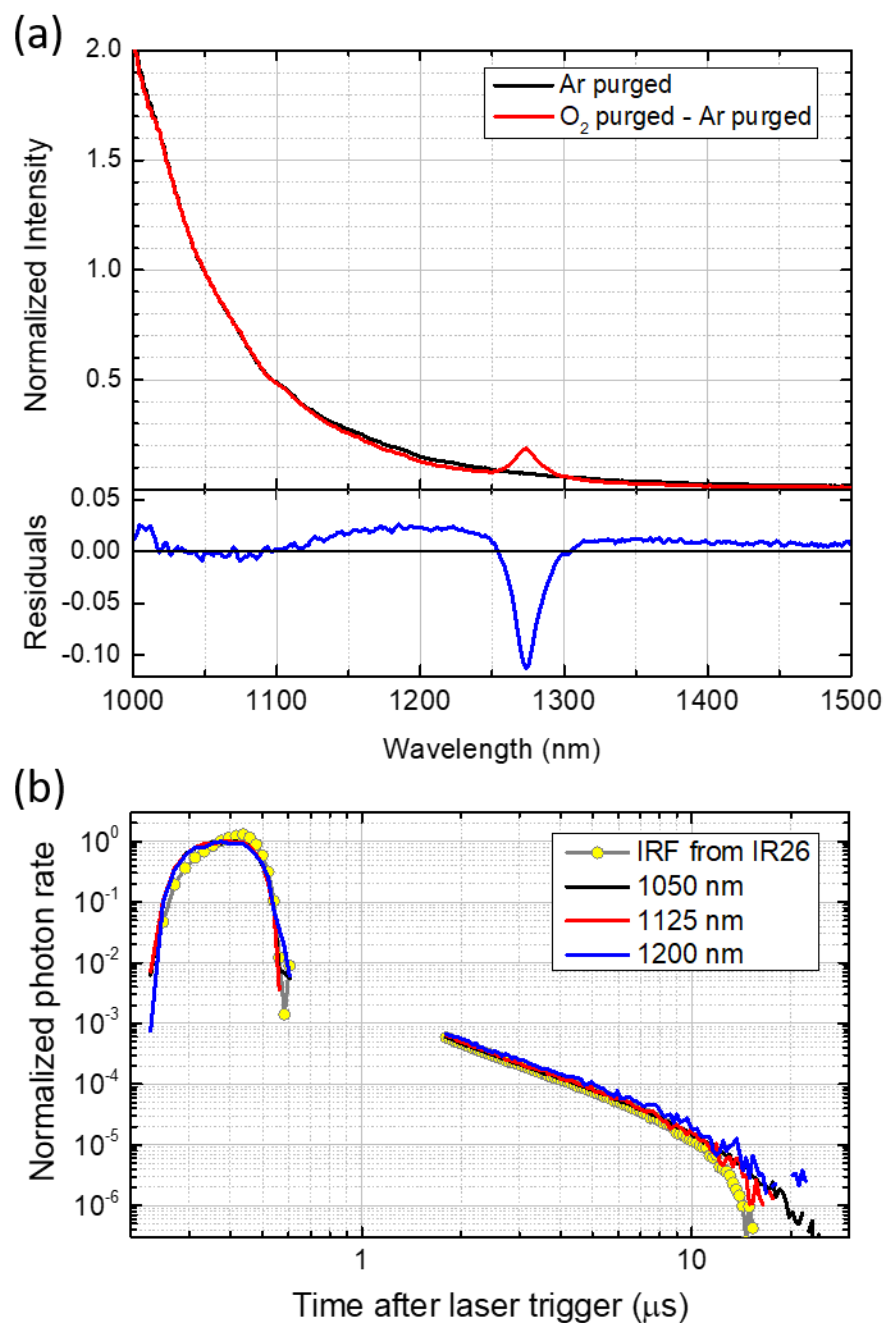
Figure S16. (a) Emission spectrum of methylene blue (MB) in O_2-saturated and Ar-saturated D_2O. Characteristic luminescence from singlet oxygen is evident near 1270 nm. (b) Normalized kinetic curves of O_2-saturated MB in D_2O compared with the normalized IRF from IR26. The strong similarity of kinetic data at 1050 nm, 1125 nm, and 1200 nm with the IRF curve suggests that the source of the tails is detector charge persistence after strong prompt luminescence in the dead period.
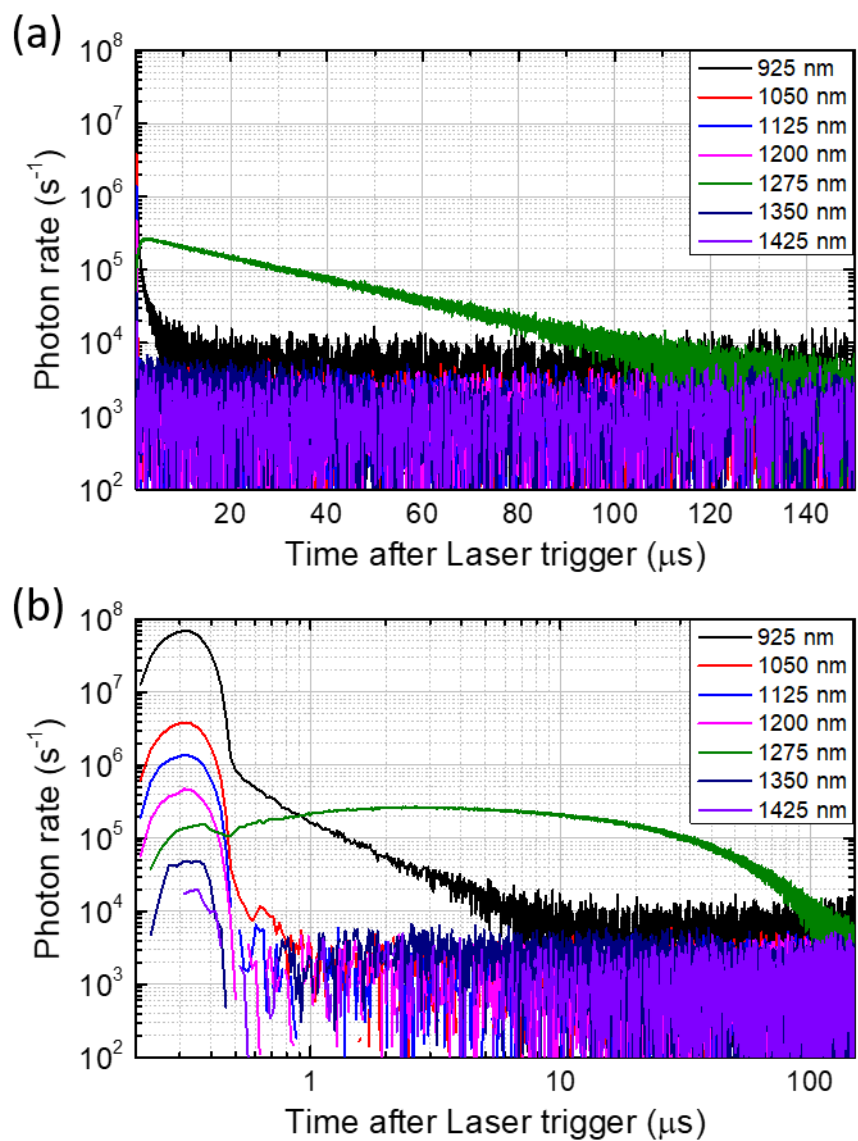
Figure S17. Spectrally-filtered SEFR-SPC kinetics from a sample of C_{70} in air-saturated toluene plotted on (a) a linear time scale, and (b) a logarithmic time scale.
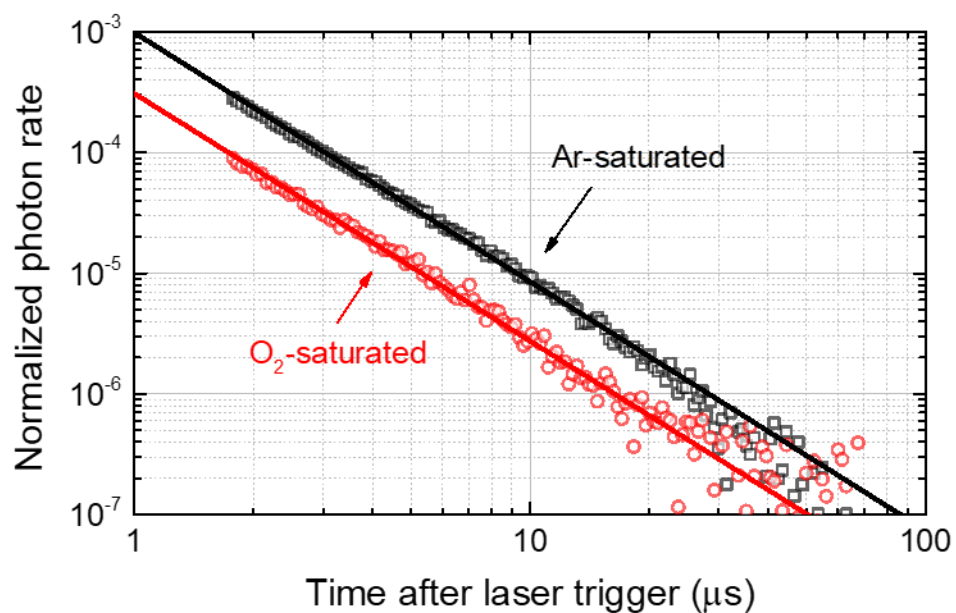
Figure S18. Delayed luminescence of PFO-coated SWCNTs in Ar- and O_2-saturated toluene. The Ar-saturated sample has intensity about 3.2 times higher than the O_2-saturated sample. The nearly linear relation in log-log plot suggests a second-order kinetic process such as triplet-triplet annihilation. Further study of this phenomenon is needed.
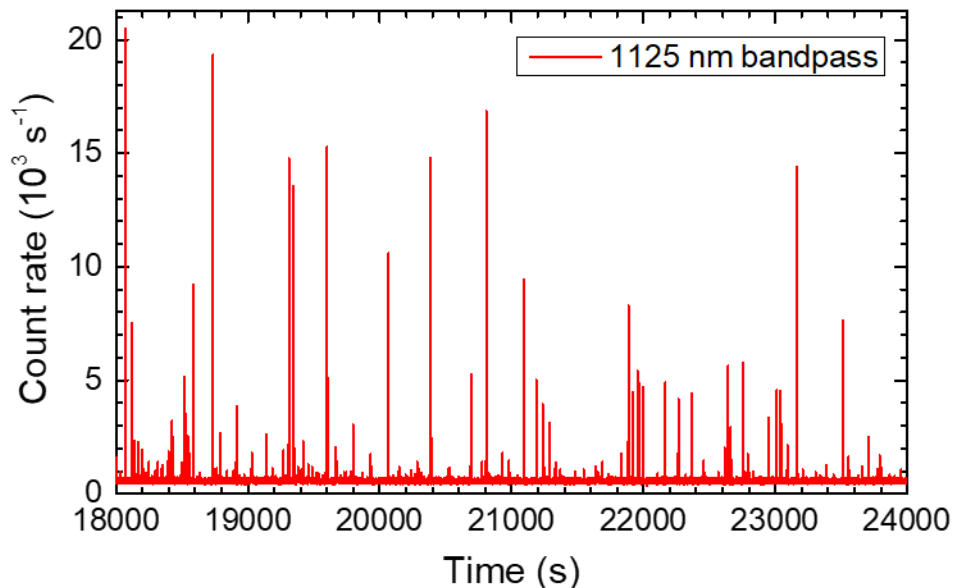
Figure S19. Single particle counting of SWCNT suspension in a flow cell using the same apparatus as for SEFR-SPC. Continuous 638 nm excitation was used. Tight focusing of excitation and collection provides the ability to resolve passages of single particles. Each spike in figure represents a SWCNT particle, most of which are thought to be individual nanotubes. The detector is sensitive enough that the low quantum yield SWCNTs still give strong signals. The physical time resolution is limited here by the detector dead time, which is from 1 to 27 μs.
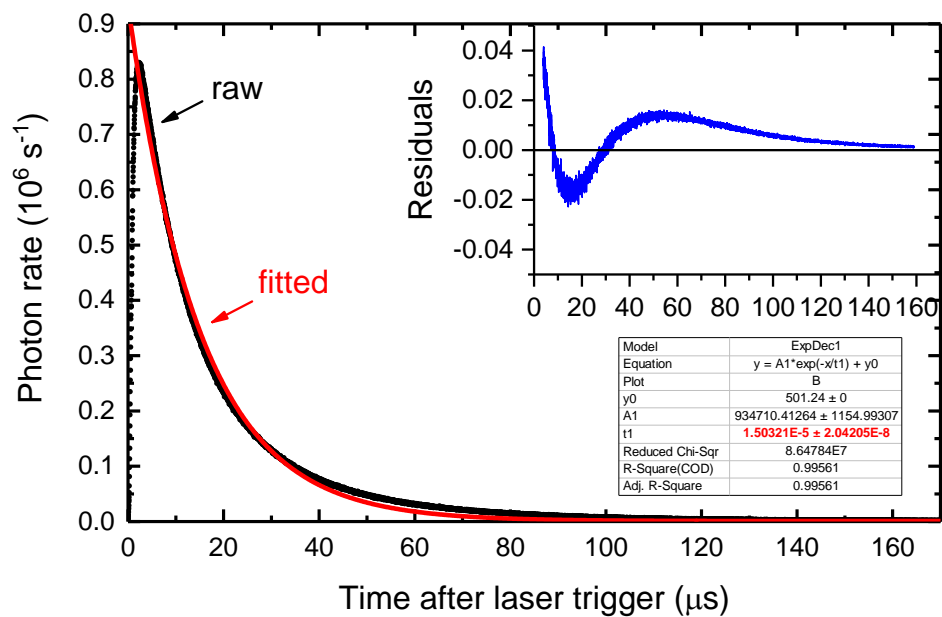
Figure S20. Simple exponential fit to the raw data for singlet oxygen decay. Inset shows the residuals of the fitted curve to the raw data.
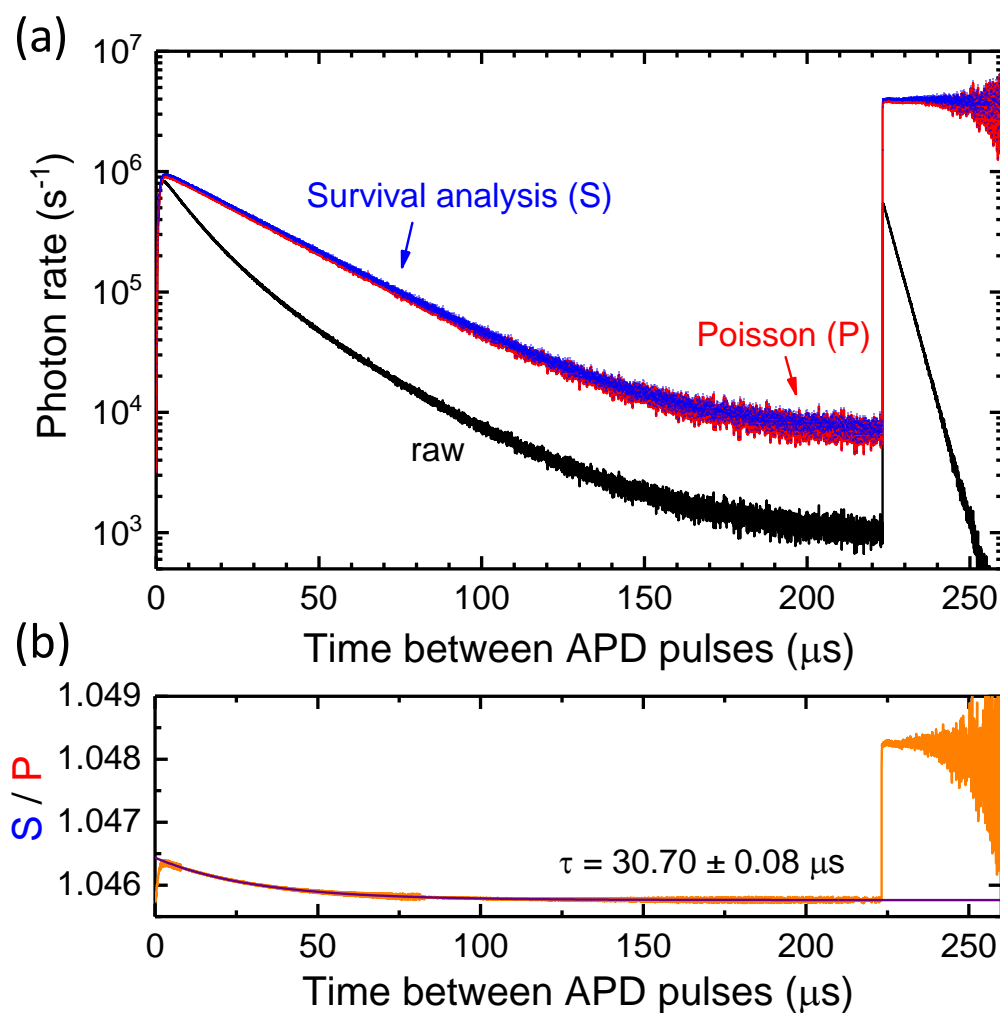
Figure S21. Comparison of the pile-up corrections from Poisson and Survival models. (a) Curves show raw data from Figure 4 (black) and the pile-up corrected curves using Survival model eq 2 (blue) and the Poisson model from literature (red). (b) The ratio of S to P (blue to red) curves. Note that the deviation of the ratio from 1 is less than 5% and nearly constant. This trace could be rather well fitted with a single exponential decay to give a decay constant near 30.7 µs, consistent with the *kt* difference noted in Table S4.

Additional Tables

Table S1. Parameters for fitting intrinsic backgrounds at different APD efficiency settings

efficiency	10%	15%	20%
Mean count rate	501.24	1054.99	2291.63
a	350.90	917.88	2165.60
b	387.55	584.25	737.46
c	95240	113950	94945
d	55.37	168.19	540.00
f	394.08	441.84	385.64
g	0	2111.9	4156.1
h	1	12.64	11.968

Table S2. Measured detector quantum efficiencies using different spectral filters and APD efficiency settings

Efficiency	10%	15%	20%
925BP150	0.0154	0.0304	0.0464
1050BP50	0.0442	0.0856	0.1230
1125BP50	0.0424	0.0806	0.1214
1200BP50	0.0470	0.0887	0.1340
1275BP50	0.0456	0.0843	0.1362
1350BP50	0.0447	0.0832	0.1343
1425BP50	0.0427	0.0790	0.1287

Table S3. Laser Pulse Energies for the Wavelengths and Pulse Durations used for Sample Excitation

Laser wavelength	Pulse energy, nJ (photon numbers, 10^{10} photons)			
	250 ns	500 ns	1 µs	2 µs
462 nm	9.66 (2.25)	49.57 (11.53)	69.81 (16.24)	87.56 (20.37)
520 nm	49.10 (12.85)	66.41 (17.39)	77.72 (20.35)	369.78 (96.80)
638 nm	13.16 (4.23)	37.72 (12.12)	61.62 (19.79)	78.57 (25.24)
660 nm	20.91 (6.95)	35.40 (11.76)	43.90 (14.59)	201.19 (66.85)
808 nm	8.22 (3.34)	20.09 (8.17)	28.92 (11.76)	129.68 (52.75)

Table S4. Comparison between reported TCSPC method and SEFR-SPC

Methods	TCSPC[2]	SEFR-SPC
theory	Poisson statistics	Survival analysis
assumptions	1. Single event per cycle 2. Large n, small p 3. Time referenced to excitation	1. Single event per cycle 2. Detector stays on until photon detected 3. Identical excitation in each cycle 4. Time referenced to APD pulses
results	General function: Not available For constant light source: $N_t = N\Delta t\lambda e^{-\lambda t}$ For single exponential decay: $N_t' = N\lambda_0\Delta t\exp\left[-\lambda_0\tau\left(1 - e^{-t/\tau}\right)\right]$	General function: $N(t,c) = ce^{-\int_0^t (K-K'/K)du}$ For constant light source: $N(t,c) = ce^{-K_0 t}$ For single exponential decay: $N(t,c) = c\cdot\exp\left[-kt + \frac{K_0}{k}\left(e^{-kt} - 1\right)\right]$
other corrections	Spectral quantum efficiency Instrument response	Dark and after-pulsing backgrounds Temporal sensitivity Spectral quantum efficiency Dynamic range Instrument response
notation	rate constant = λ_0; decay time = τ	rate constant = k; decay time = $1/k$

References

(1) Thew, R. T.; Stucki, D.; Gautier, J. D.; Zbinden, H.; Rochas, A. Free-running InGaAs/InP avalanche photodiode with active quenching for single photon counting at telecom wavelengths *Appl. Phys. Lett.* **2007**, *91*, 201114.

(2) Holzapfel, C. On statistics of time-to-amplitude converter systems in photon counting devices *Rev. Sci. Instrum.* **1974**, *45*, 894-896.

(3) Dalla Mora, A.; Contini, D.; Pifferi, A.; Cubeddu, R.; Tosi, A.; Zappa, F. Afterpulse-like Noise Limits Dynamic Range in Time-gated Applications of Thin-junction Silicon Single-photon Avalanche Diode *Appl. Phys. Lett.* **2012**, *100*, 4.

(4) Dalla Mora, A.; Tosi, A.; Contini, D.; Di Sieno, L.; Boso, G.; Villa, F.; Pifferi, A. Memory Effect in Silicon Time-gated Single-photon Avalanche Diodes *J. Appl. Phys.* **2015**, *117*, 7.

(5) Kopainsky, B.; Qiu, P.; Kaiser, W.; Sens, B.; Drexhage, K. H. Lifetime, photostability, and chemical structure of IR heptamethine cyanine dyes absorbing beyond 1 μm *Applied Physics B* **1982**, *29*, 15-18.

(6) Stich, D.; Spath, F.; Kraus, H.; Sperlich, A.; Dyakonov, V.; Hertel, T. Triplet-triplet Exciton Dynamics in Single-walled Carbon Nanotubes *Nat. Photonics* **2014**, *8*, 139-144.

(7) Becker, W. *Advanced Time-correlated Single Photon Counting Techniques*; Springer Science & Business Media, 2005; Vol. 81.

(8) Léonard, J.; Dumas, N.; Caussé, J.-P.; Maillot, S.; Giannakopoulou, N.; Barre, S.; Uhring, W. High-throughput time-correlated single photon counting *Lab Chip* **2014**, *14*, 4338-4343.

(9) Sergent, N.; Levitt, J. A.; Green, M.; Suhling, K. Rapid Wide-field Photon Counting Imaging with Microsecond Time Resolution *Opt. Express* **2010**, *18*, 25292-25298.

(10) Hirvonen, L. M.; Festy, F.; Suhling, K. Wide-field time-correlated single-photon counting (TCSPC) lifetime microscopy with microsecond time resolution *Opt. Lett.* **2014**, *39*, 5602-5605.

(11) Donohue, D. E.; Stern, R. C. Correction of Single Photon or Particle Timing Measurements for Multiparticle Events *Rev. Sci. Instrum.* **1972**, *43*, 791-796.

(12) Rodríguez, G., 2007.

(13) Meurs, B. v.; Werf, R. v. d. A Circuit for Rejecting Multiple Events Detected during a Timing Cycle in Single Photon Counting Experiments *J. Phys. E: Sci. Instrum.* **1976**, *9*, 437-438.

(14) Salthammer, T. Numerical Simulation of Pile-up Distorted Time-correlated Single Photon Counting (TCSPC) Data *J. Fluoresc.* **1992**, *2*, 23-27.

(15) Coates, P. B. Pile-up Corrections in the Measurement of Lifetimes *J. Phys. E: Sci. Instrum.* **1972**, *5*, 148-150.

(16) Coates, P. B. The Correction for Photon 'Pile-up' in the Measurement of Radiative Lifetimes *J. Phys. E: Sci. Instrum.* **1968**, *1*, 878.

(17) Arlt, J.; Tyndall, D.; Rae, B. R.; Li, D. D.-U.; Richardson, J. A.; Henderson, R. K. A Study of Pile-up in Integrated Time-correlated Single Photon Counting Systems *Rev. Sci. Instrum.* **2013**, *84*, 103105.

(18) Harris, C.; Selinger, B. Single-Photon Decay Spectroscopy. II. The Pile-up Problem *Aust. J. Chem.* **1979**, *32*, 2111-2129.

(19) Coates, P. B. Pile-up Corrections in Lifetime Experiments *Rev. Sci. Instrum.* **1972**, *43*, 1855-1856.

(20) Davis, C. C.; King, T. A. Single Photon Counting Pileup Corrections for Time-Varying Light Sources *Rev. Sci. Instrum.* **1970**, *41*, 407-408.

(21) Davis, C. C.; King, T. A. Correction Methods for Photon Pile-up in Lifetime Determination by Single-photon Counting *J. Phys. A: Gen. Phys.* **1970**, *3*, 101-109.

(22) Coates, P. B. PILE-UP CORRECTIONS IN LIFETIME EXPERIMENTS *Rev. Sci. Instrum.* **1972**, *43*, 1855-&.

(23) Davis, C. C.; King, T. A. Photon Pile-up Corrections in the Study of Time-varying Light Sources *J. Phys. E: Sci. Instrum.* **1972**, *5*, 1072-1074.